

Article

Corrosion Resistance of CoCrFeNiMn High Entropy Alloy Coating Prepared through Plasma Transfer Arc Claddings

Pei-Hu Gao^{1,2,*} , Rui-Tao Fu^{1,2}, Bai-Yang Chen¹, Sheng-Cong Zeng¹, Bo Zhang¹, Zhong Yang^{1,2}, Yong-Chun Guo^{1,2}, Min-Xian Liang^{1,2}, Jian-Ping Li^{1,2,*}, Yong-Qing Lu³, Lu Jia³ and Dan Zhao³

- ¹ School of Materials and Chemical Engineering, Xi'an Technological University, Xi'an 710021, China; ruitaofu@163.com (R.-T.F.); baiyang2578@163.com (B.-Y.C.); Z18889918364@163.com (S.-C.Z.); bozhang@163.com (B.Z.); yz750925@163.com (Z.Y.); yc_guo@163.com (Y.-C.G.); lingmx@163.com (M.-X.L.)
- ² Shaanxi Province Engineering Research Centre of Aluminum/Magnesium Light Alloy and Composites, Xi'an 710021, China
- ³ Shanxi Diesel Engine Co., Ltd., Datong 035600, China; luyq@163.com (Y.-Q.L.); jialu@163.com (L.J.); zhaodan@163.com (D.Z.)
- * Correspondence: tigergaopei@163.com (P.-H.G.); lijianping@mail.xatu.edu.cn (J.-P.L.); Tel.: +86-29-8320-8080 (P.-H.G.); +86-29-8617-3324 (J.-P.L.)

Abstract: High entropy alloy attracts great attention for its high thermal stability and corrosion resistance. A CoCrFeNiMn high-entropy alloy coating was deposited on grey cast iron through plasma transfer arc cladding. It formed fine acicular martensite near the grey cast iron, with columnar grains perpendicular to the interface between the grey cast iron substrate and the cladding layer as well as dendrite in the middle part of the coatings. Simple FCC solid solutions present in the coatings which were similar to the powder's structure. The coating had a microhardness of $300 \pm 21.5 \text{ HV}_{0.2}$ when the cladding current was 80 A for the solid solution strengthening. The HEA coating had the highest corrosion potential of -0.253 V when the plasma current was 60 A, which was much higher than the grey cast iron's corrosion potential of -0.708 V . Meanwhile, the coating had a much lower corrosion current density of $9.075 \times 10^{-7} \text{ mA/cm}^2$ than the grey cast iron's $2.4825 \times 10^{-6} \text{ mA/cm}^2$, which reflected that the CoCrFeNiMn HEA coating had much better corrosion resistance and lower corrosion rate than the grey cast iron for single FCC solid solution phase and a relatively higher concentration of Cr in the grain boundaries than in the grains and this could lead to corrosion protection effects.

Keywords: high-entropy alloy coating; plasma cladding; microstructure; corrosion



Citation: Gao, P.-H.; Fu, R.-T.; Chen, B.-Y.; Zeng, S.-C.; Zhang, B.; Yang, Z.; Guo, Y.-C.; Liang, M.-X.; Li, J.-P.; Lu, Y.-Q.; et al. Corrosion Resistance of CoCrFeNiMn High Entropy Alloy Coating Prepared through Plasma Transfer Arc Claddings. *Metals* **2021**, *11*, 1876. <https://doi.org/10.3390/met11111876>

Academic Editor: Mirosław Szala

Received: 31 October 2021

Accepted: 20 November 2021

Published: 22 November 2021

Publisher's Note: MDPI stays neutral with regard to jurisdictional claims in published maps and institutional affiliations.



Copyright: © 2021 by the authors. Licensee MDPI, Basel, Switzerland. This article is an open access article distributed under the terms and conditions of the Creative Commons Attribution (CC BY) license (<https://creativecommons.org/licenses/by/4.0/>).

1. Introduction

In 2004, the Taiwanese scholars JYeh et al. [1] broke through the traditional concept of material design and proposed a new alloy design concept to prepare multi-principal high-entropy alloys. The HEAs consists of five or more principal elements in equal or near-equal atomic percentages [2]. Moreover, HEAs generally have a simple-phase solid solution structure. This area has been greatly developed. It is easy to obtain solid solutions, nanostructures and even amorphous structures for HEAs because they have high configurational entropy. Meanwhile, atoms are not easily diffused in HEAs. As a result, HEAs exhibit many excellent properties such as ultrahigh strength [3,4], high ductility [5], exceptional catalytic performance [6], outstanding irradiation resistance [7], high corrosion resistance [8] and excellent wear resistance [9]. Among the large number of high entropy alloys, the equiatomic CoCrFeNiMn HEAs have attracted more and more interest for their stable single face centered cubic (FCC) structure [10,11].

So far, high entropy alloys are mainly melted in a vacuum arc furnace. During vacuum melting, the alloy materials experience a high heating temperature for a long heating time. Since most high entropy alloys contain relatively expensive metals such as cobalt, nickel,

chromium and so on, the costs of high entropy alloy bulks are very high. Compared with high entropy alloy bulks, high entropy alloy coatings can increase the utilization rate of the alloy and lower the costs. Therefore, high entropy alloy coatings have good prospects in engineering applications and have attracted considerable attention in recent years.

The methods used to prepare HEA coatings include electrochemical deposition, magnetron sputtering [12], thermal spraying [13,14], laser cladding [15] and so on. Ye et al. [16] manufactured a novel $\text{Al}_x\text{FeCoNiCuCr}$ high-entropy alloy coating with high hardness and good abrasion resistance and corrosion resistance through laser cladding. The $\text{Al}_x\text{FeCoNiCrTi}$ coatings prepared by laser cladding, among which $\text{Al}_{1.8}\text{FeCoNiCrTi}$ was the best, performed much better than 314L stainless steel in corrosion resistance, Lehtonen et al. [17] reported the deposition of CrFeNiMn by cold spraying. Chen et al. [18] prepared a $\text{Al}_{10.6}\text{TiCrFeCoNi}$ high-entropy alloy coating with a dense microstructure, two BCC phases with similar lattice parameters, a high microhardness of $789 \pm 54 \text{ HV}_{0.2}$ and good fracture toughness of $8.4 \text{ MPa}\cdot\text{m}^{1/2}$ by HVOF spraying. Zhang et al. [19] prepared an amorphous FeCrMnWMoSi coating with lower porosity and superior electrochemical corrosion resistance by high velocity oxygen-fuel spraying technology. Zhang et al. [20] reported that the wear resistance of $(\text{CuCoCrFeNi})_{95}\text{B}_5$ high-entropy alloy coating prepared by plasma cladding technology was 2.3 times that of a Q235 steel substrate. Kim et al. [21] and Wang et al. [22] used magnetron sputtering and electrochemical deposition to prepare $\text{Al}_x\text{CoCrFeNi}$ and CuNiSiTiZ high-entropy alloy coatings. The coatings had a compact structure and high hardness. However, magnetron sputtering and electrochemical deposition were only suitable for preparing thin-film coatings, and the bonding force between the coating and the substrate was relatively poor. A plasma transfer arc has higher energy density than a thermal spray, but lower energy density than a laser. Therefore, it provided relatively low thermal deformation of the substrate, low dilution and good metallurgical bonding between the coating and substrate [23,24]. Hence, plasma transfer arc cladding is seen as an effective method to prepare thick high-entropy alloy coatings.

Grey cast iron is often used for engine parts. It is easily corroded due to its biphasic composite structure with free carbon as corrosion channel. HEA coatings could be an effective way of providing corrosion resistance for grey cast iron.

In this paper, CoCrFeNiMn coatings were prepared on the surface of grey cast iron using plasma transfer arc cladding technology to protect the grey cast iron substrate from corrosion. The effect of the plasma transfer arc current on the microstructure and corrosion resistance of CoCrFeNiMn high-entropy alloy coating was investigated.

2. Materials and Methods

2.1. Powder and Coating Deposition

The adopted CoCrFeNiMn powder was produced by AVIMETAL Powder Metallurgy Co., Ltd. (Beijing, China). The feedstock was an equiatomic CoCrFeNiMn HEA powder with a spherical morphology, as shown in Figure 1. The feedstock size distribution ranged from 15 to 53 μm . The composition of the feedstock is listed in Table 1. The powder had near-equiatomic percentages. Figure 2 shows the X-ray diffraction pattern of the powder. The powder had a single phase with a face centered cubic (FCC) structure. The CoCrFeNiMn HEA coating was deposited on the grey cast iron with a size of 100 mm \times 100 mm \times 10 mm through a PTA system (DML-V03BD, Shanghai Dom Machinery Co., Ltd., Shanghai, China). The grey cast iron substrate surface was prepared by cleaning with acetone before coating. Figure 3 shows the microstructure of the substrate, which is composed of flake graphite and pearlite. Table 2 shows the chemical composition of the grey cast iron. During the plasma cladding, argon was chosen as shielding gas and hydronium gas. The plasma torch was kept 10 mm from the torch exit to the substrate and the travelling speed was kept at 150 mm/min within the operation of a six-axis robot (HP-20D, Yaskawa, Kitakyushu, Japan). The ion gas flow and the protection gas flow were 1.5 L/min and 10 L/min, respectively. The powder feeding rate was kept at 20 r/min. The plasma arc currents were 50, 60, 70 and 80 A. Table 3 lists the plasma cladding parameters.

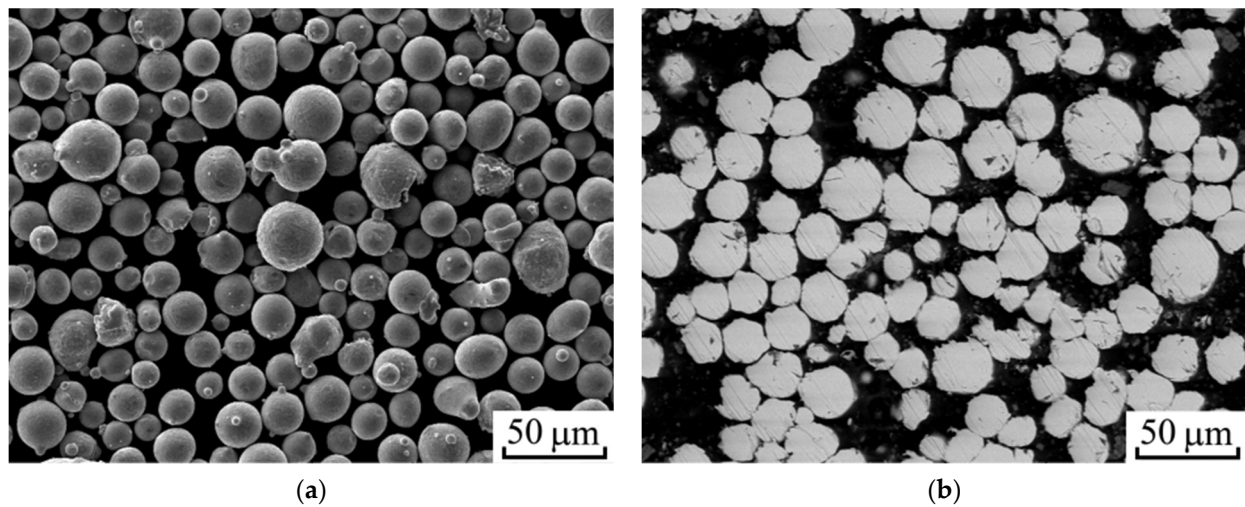


Figure 1. Microstructure of CoCrFeNiMn powder: (a) global morphology, (b) cross-sectional microstructure.

Table 1. Composition of the CoCrFeNiMn high entropy alloy powder.

Element	Co	Cr	Fe	Ni	Mn
wt.%	20.58	18.35	19.98	20.49	20.48

Table 2. Composition of the grey cast iron.

Element	C	Si	Mn	Cu	Sn	S	Fe
wt.%	3.3	2.0	0.45	0.5	0.1	0.05	balance

Table 3. Parameters of plasma cladding.

Plasma Arc (A)	Scanning Speed (mm/min)	Ion Gas Flow (L/min)	Protection Gas Flow (L/min)	Powder Feeding Rate (rad/min)	Distance from Torch Exit to Substrate (mm)
50, 60, 70, 80	150	1.5	10	20	10

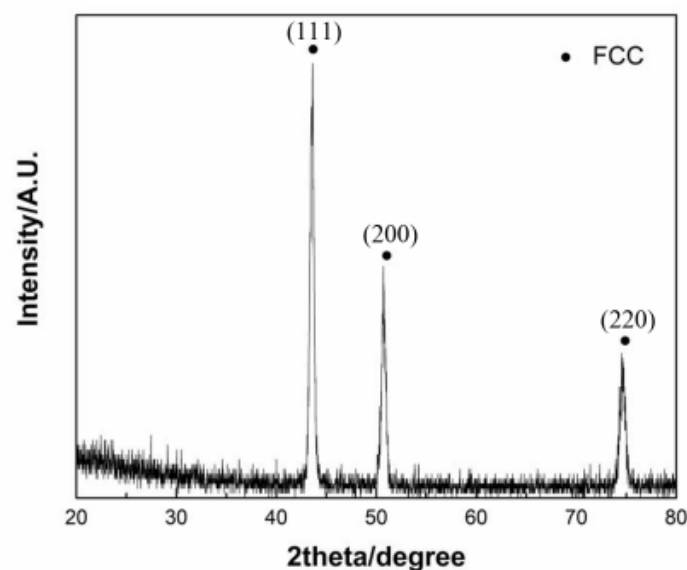


Figure 2. XRD pattern of CoCrFeNiMn powder.

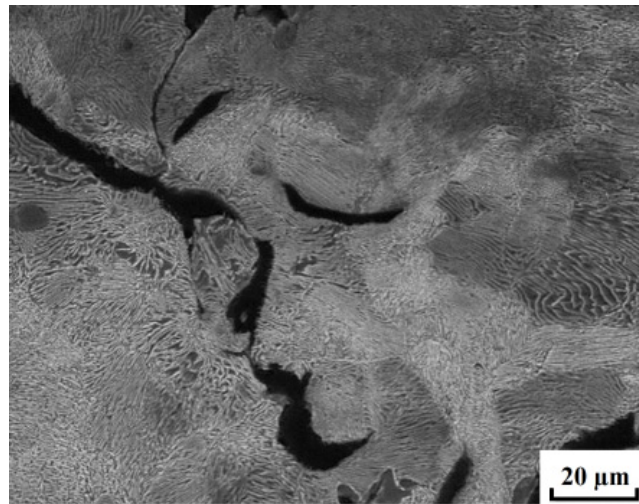


Figure 3. Microstructure of the grey cast iron.

2.2. Microstructure Characterization

The powder and coatings were characterized by scanning electron microscopy (SEM, VEGA II-XMU, TESCAN, Brno, Czech Republic) with EDX (7718, Oxford Instruments, Abingdon, UK). The sample was etched with a 10% nitric acid alcohol solution for 3 s. The phases of powders and coatings were analyzed by X-ray diffraction (XRD-6000, Shimadzu, Kyoto, Japan) using Cu K α radiation. The test was performed with a step of 0.02° from 20° to 80° at a scanning speed of 2°/min. The micro-hardness of the coating was measured by a Vickers micro-hardness tester (HV-5, Taiming, Shanghai, China) under a load of 200 gf for a loading duration of 30 s. The microhardness was tested ten times for each sample and the mean microhardness was calculated. Meanwhile, the interval between the adjacent indentation was controlled to be twice larger than the single indentation size to avoid the deformation from affecting of the impression process.

2.3. Electrochemical Characterization

The corrosion resistance of the coatings was tested and analyzed using a Princeton electrochemical workstation (PARTAT 4000 electrochemical workstation, Princeton Applied Research, Princeton, NJ, USA). Open circuit potential, impedance test, and dynamic potential polarization curve tests were performed sequentially. Generally, the exposed area for the electrochemical test was controlled to 10 mm \times 10 mm. While, for the convenient testing of the single-track cladding layer, the size of the electrochemical test sample was 4 mm \times 4 mm \times 1.2 mm. Copper wire was soldered to the back of the sample and the sample was encapsulated with resin. The surface of the HEA coating of size 4 mm \times 4 mm was exposed, sanded and polished with 2000 grit paper before the electrochemical test. The corrosion current density of the HEA coatings was calculated on the corrosion surface of 4 mm \times 4 mm. The testing accuracy of the samples in 4 mm \times 4 mm was in consistent with that in 10 mm \times 10 mm. The test was performed in a typical three-electrode electrochemical method with dynamic potential polarization. The experiment was performed with 3.5% NaCl solution as the electrolytic cell solution, platinum electrode for the auxiliary stage, and saturated calomel electrode (SCE) for the reference electrode (saturated KCl solution was added to the saturated calomel electrode). The test time was set to 3600 s to ensure that a stable open circuit potential was obtained. The polarization curve scan rate was 2 mV/s. The impedance frequency range was 10 kHz~100 MHz and the amplitude was 5 mV.

The equivalent circuit diagram was fitted using ZView software[®] and the polarization resistance R_p was calculated by the Stern-Geary equation [25]:

$$R_p = \frac{\beta_\alpha \times \beta_c}{2.3 \times I_{corr} \times (\beta_\alpha + \beta_c)} \quad (1)$$

where β_α and β_c are the cathodic Tafel slope and the anodic Tafel slope, respectively, and I_{corr} is the corrosion current density.

3. Results and Discussions

3.1. Microstructure of the HEA Coatings

Figure 4 shows the microstructure of the plasma-cladded CoCrFeNiMn high-entropy alloy coating at 70 A current. As seen in Figure 4a, the global HEA coating bonded with the grey cast iron very well without cracks, and contained four parts, including a coating zone (CZ), bonding zone (BZ), heat affected zone (HAZ) and substrate zone (SZ). Fine acicular martensite (M, labeled by an arrow) was formed near the grey cast iron, which reflected that there were some parts that remelted on the surface of the grey cast iron during plasma transfer arc cladding, as seen in Figure 4b. Besides martensite and the HEA coating, there existed ledeburite (L) in the upper part of the bonding zone. During the remelting of the grey cast iron surface, some of the remelting material cooled quickly to form martensite (M) while the rest cooled and mixed with HEA melt to form ledeburite (L). Nevertheless, there was a strong metallurgical bonding between the coating and the substrate.

In the coating zone, as shown in Figure 4c, there were columnar grains perpendicular to the bonding interface, which was closely related to the temperature distribution during plasma heating and cooling. The coating zone was mainly composed of dendritic forms. With the increase of the plasma current, the molten pool temperature increased. The HEA melt's heat transferred towards both the grey cast substrate and the upper surface near to the air. Therefore, the heat flow was perpendicular to the grey cast iron substrate which led to columnar grains parallel to the heat flow and perpendicular to the substrate. In the HEA coating's top edge zone, the coating at the edge cooled finally to form equiaxial grains as shown in Figure 4d.

Figure 5 shows the point analysis of the elements in the CoCrFeNiMn HEA coating prepared at 70 A plasma arc current. The contents of Co and Cr in the grain boundaries were higher than those in the grains. The contents of Ni and Mn in the grains were higher than those in the grain boundaries. Meanwhile, carbon was found both in the grains and grain boundaries, which might be related to the dilution of the melting surface of the grey cast iron. The iron contents were higher in both the grains and the grain boundaries than the powders, which on the other hand demonstrated the dilution of the melting surface of the grey cast iron. Meanwhile, the contents of cobalt, nickel and manganese were lower in both the grains and the grain boundaries than the powders. During the quick melting of the HEA powders, there were burning losses of cobalt, nickel and manganese, which might be related to their relatively low saturated vapor pressure [26]. Oxides were found in the grain boundaries. The oxygen content was 4.05% (wt) through EDX point analysis as shown in Figure 5b,c and Table 4. In addition, there was no oxygen in the grains. Meanwhile, the content of manganese in the grains was higher than that in the grain boundaries. Manganese had a strong slag removal ability. During the melting of HEA powder, oxidation might occur on the surface of the powder. Figure 6 shows the EDX maps of elements in the middle part of the CoCrFeNiMn coating prepared at 70 A plasma arc current. Co and Cr were enriched in the grain boundaries, Ni and Mn were concentrated in the grains, which corresponded with the point analysis results. Iron was distributed uniformly, and no obvious differences between the grain and grain boundaries could be found. Meanwhile, oxygen was mainly distributed along the boundaries of the gains, which demonstrated that oxidation occurred on the surface of the powder during the cladding process.

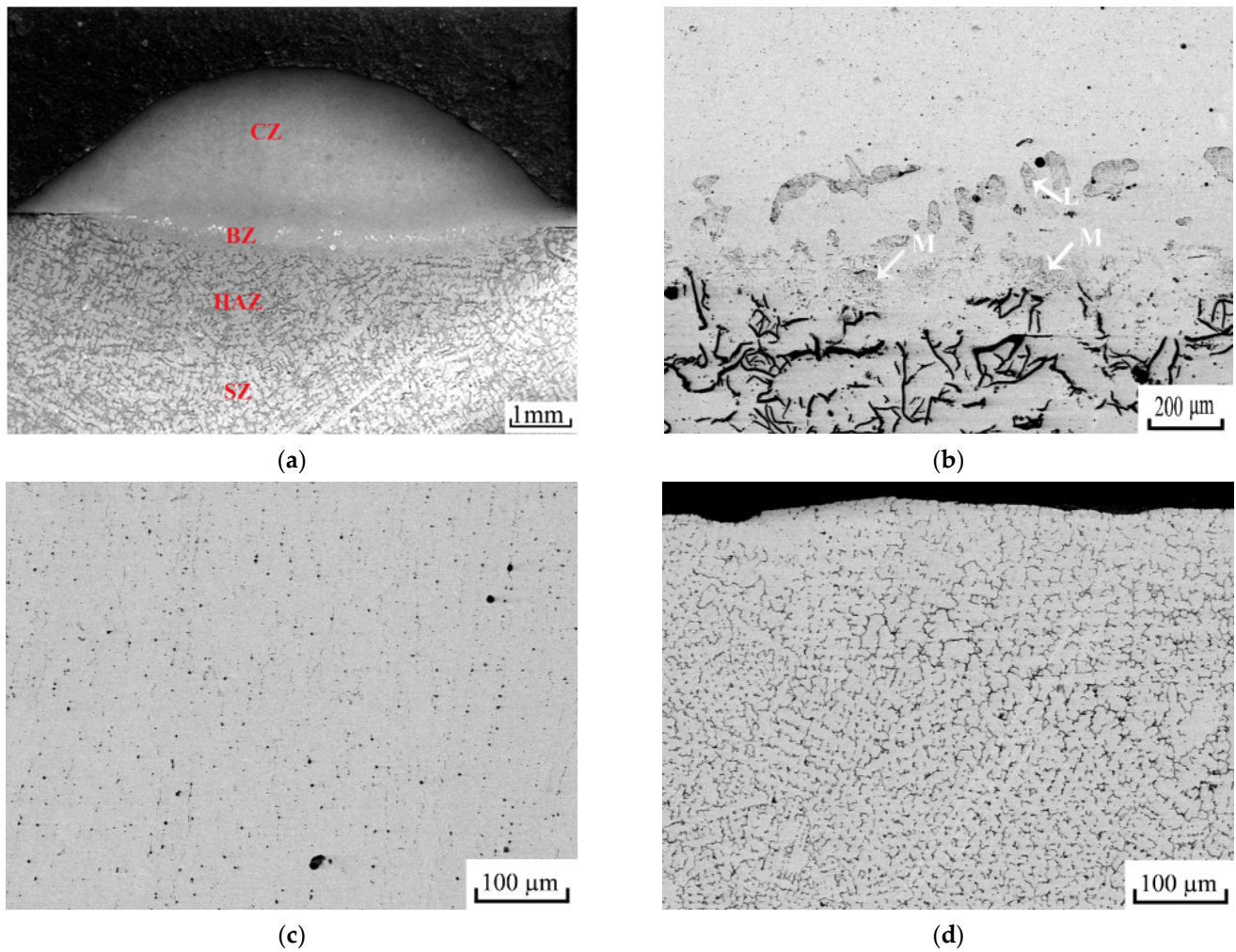


Figure 4. Cross-sectional microstructure of CoCrFeNiMn HEA coating at 70A plasma current: (a) global morphology with coating zone (CZ), bonding zone (BZ), heat affected zone (HAZ) and substrate zone (SZ), (b) bonding zone with martensite (M) and ledeburite (L), (c) coating zone, (d) coating zone after deep etching.

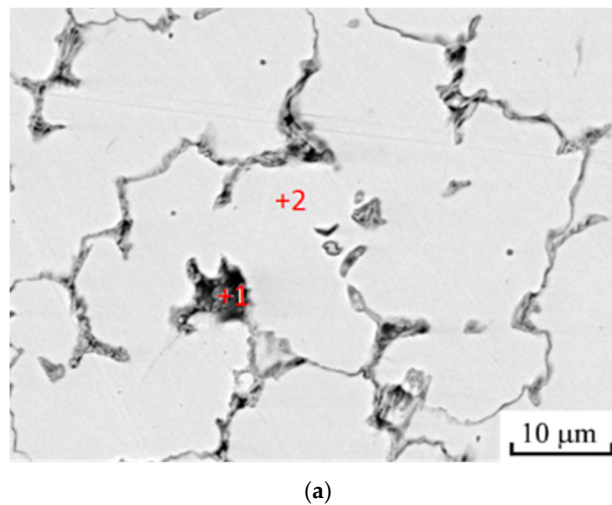


Figure 5. Cont.

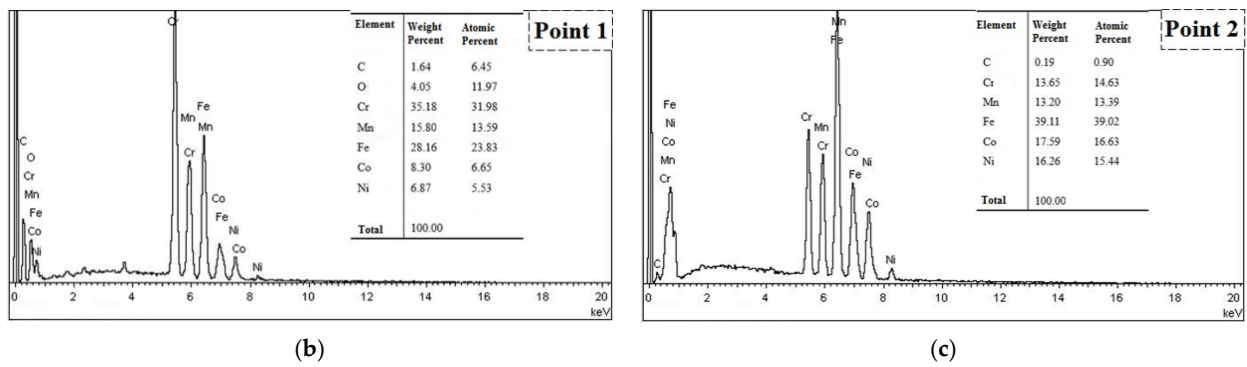


Figure 5. Point analysis of elements in CoCrFeNiMn coating prepared at 70 A plasma current: (a) coating, (b) composition of point 1, (c) composition of point 2.

Table 4. Composition of the CoCrFeNiMn high entropy alloy powder and point analysis of elements in the HEA coating prepared at 70 A plasma arc current.

Element (wt.%)	C	O	Co	Cr	Fe	Ni	Mn
Powder	-	-	20.58	18.35	19.98	20.49	20.48
Point 1	1.64	4.05	35.18	15.80	28.16	8.30	6.87
Point 2	0.19	-	13.65	13.20	39.11	17.59	16.26

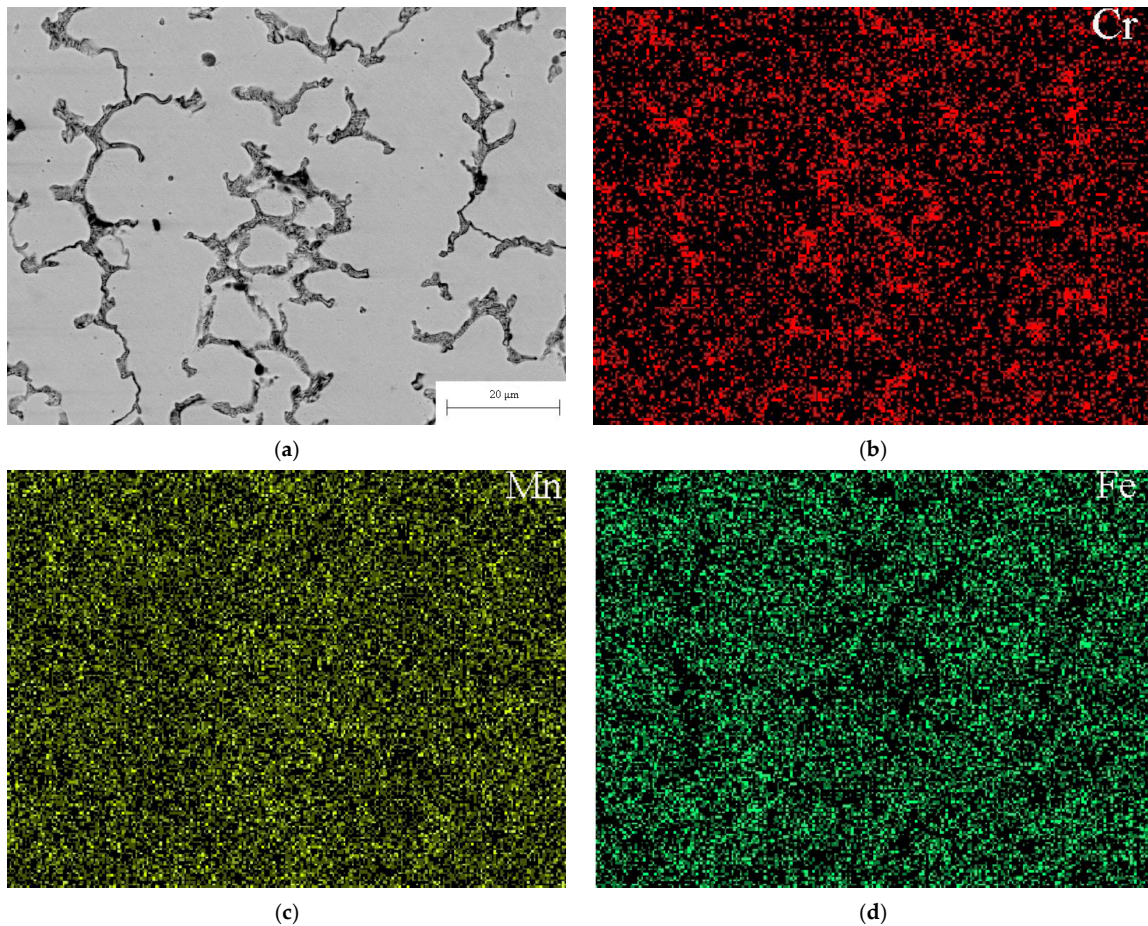


Figure 6. Cont.

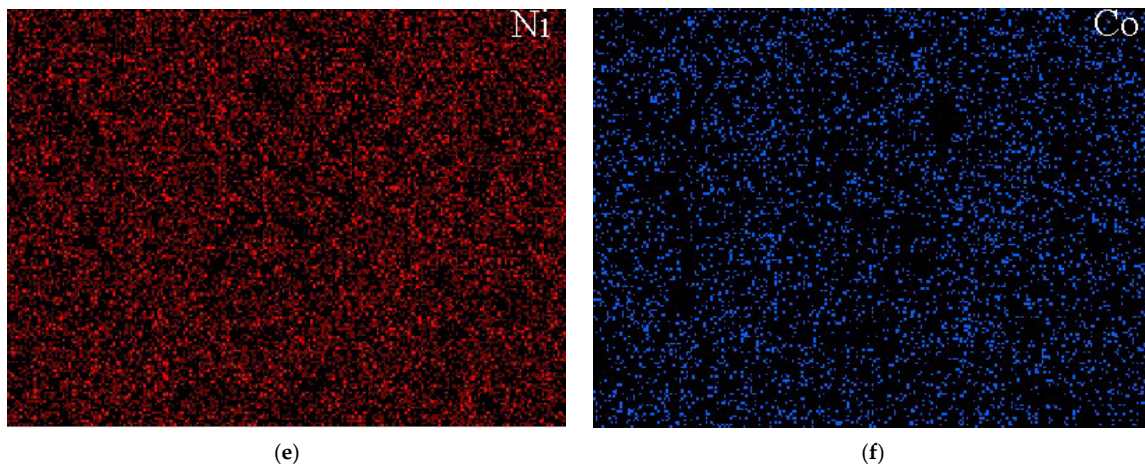


Figure 6. EDX maps of elements in the middle part of the CoCrFeNiMn coating prepared at 70 A plasma arc current: (a) microstructure; (b) Cr distribution; (c) Mn distribution; (d) Fe distribution; (e) Ni distribution; (f) Co distribution.

3.2. Phases

Figure 7 shows the X-ray diffraction patterns of CoCrFeNiMn HEA coatings prepared by plasma transfer arc cladding at different plasma currents. It was found that CoCrFeNiMn HEA coatings mainly had three characteristic peaks at 43.23° , 52.69° and 73.60° . According to the research results of references [27] and PDF cards (PDF card No. 33-0397), the characteristic peaks corresponded to the (111), (200) and (220) lattice planes of face centered cubic (FCC) solid solutions, respectively. Therefore, the HEA coatings consisted of a single FCC phase, which was similar to the single FCC phase of FeCrNiCo high entropy alloy coating reported in Zhang's work [28]. The formation of a single FCC structure could be related to the fact that the elements selected for the preparation of the alloys were all adjacent elements of the fourth period and their atomic radii were similar [29]. According to the Gibbs phase ratio [30], the number of equilibrium solidification phases of n elements is $p = n + 1$, and the number of non-equilibrium solidification phases is $p > n + 1$. It could be found from Figure 7 that the phase number of CoCrFeNiMn HEA coating was one, which was less than six. Since the CoCrFeNiMn HEA had a high mixing entropy, the formation of common intermetallic compounds was inhibited. No oxide peaks were found in the XRD patterns. Although there were oxides in the grain boundaries, oxidation did not occur in the HEA grains. The amount of the oxides in the grain boundaries was too little to be detected by X-ray diffraction. Meanwhile, Mn element in the powder displayed a strong deoxidation and slagging effect during plasma melting. Simultaneously, the argon used could protect from oxidation too [31].

Table 5 shows the lattice parameters of the CoCrFeNiMn HEA powder and coatings prepared at different plasma arc currents calculated from the X-ray diffraction patterns through MDI Jade software[®]. With the increase of plasma arc current, the lattice parameters of the CoCrFeNiMn HEA coatings decreased, but, most of the four HEA coatings had larger lattice parameters than the powder, except the HEA coating prepared at 80 A plasma arc current. With the increase of plasma arc current, the heat input in the plasma cladding process increased greatly, which led to fast heating and cooling speed simultaneously. The super cooling effect led to great solid solution and finally to larger lattice parameters in the CoCrFeNiMn HEA coatings than that in the powder, especially at 50, 60 and 70 A plasma arc currents, while, the cooling times became longer and longer with the increase of the plasma arc current. A dynamic equilibrium process would exist between the solid solution and de-solution, which was affected by both the cooling speed and time. Although the cooling speed increased with the increase of plasma arc current, the cooling times were extended obviously, which brought much more chances for de-solution to happen.

Therefore, the lattice parameters of the CoCrFeNiMn HEA coating prepared at 80 A plasma arc current were a little smaller than those of the powder.

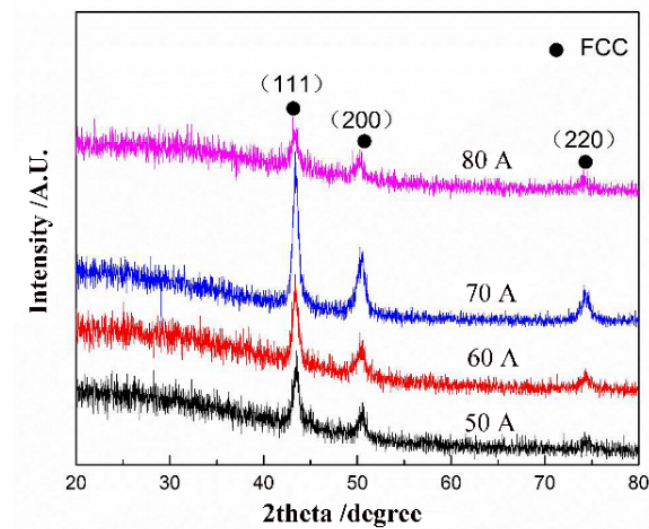


Figure 7. XRD patterns of the HEA coatings.

Table 5. Lattice parameters of the CoCrFeNiMn HEA powder and coatings prepared at different plasma arc currents.

Lattice Parameters	Powder	Coatings			
		50 A	60 A	70 A	80 A
Å	3.59751 ± 0.00018	3.60495 ± 0.00021	3.59809 ± 0.00017	3.59778 ± 0.00019	3.59709 ± 0.00018

3.3. Microhardness

Figure 8 shows the microhardness of the CoCrFeNiMn HEA coatings. Figure 8a shows the microhardness distribution along the upper surface of the HEA coating cross-section to the substrate. The microhardness of the HEA coating increased with the increase of the plasma arc current. The highest microhardness of the HEA coating was $300 \pm 21.5 \text{ HV}_{0.2}$ when the plasma current was 80 A for the solid solution strengthening. The lowest microhardness of the HEA coating was $203.3 \pm 7.2 \text{ HV}_{0.2}$ when the plasma current was 50 A, which was comparable to the microhardness of grey cast iron. Table 6 shows the grain width of dendritic structure at different plasma currents. With the increase of plasma current, the width of dendrites in the coating became small, which would produce a fine grain strengthening effect.

When the microhardnesses of the bonding zone (BZ) and heat affected zone (HAZ) were compared, the microhardnesses of the bonding zone (BZ) and heat affected zone (HAZ) varied from $600 \text{ HV}_{0.2}$ to $700 \text{ HV}_{0.2}$, which are much higher than those of both the HEA coatings and the grey cast iron as seen in Figure 8b. In the bonding zone (BZ), there were comixed CoCrFeNiMn HEA solid solutions, ledeburite (L) and fine acicular martensite (M) formed near the grey cast iron for some parts remelted at fast heating and cooling speed on the surface of the grey cast iron during plasma transfer arc cladding, which led to a great increase of the microhardness in the bonding zone (BZ). Meanwhile, in the heat affected zone (HAZ), the pearlite (P) in the grey cast iron substrate was heated and cooled quickly and changed to martensite (M) with high hardness, which had been previously reported [32,33].

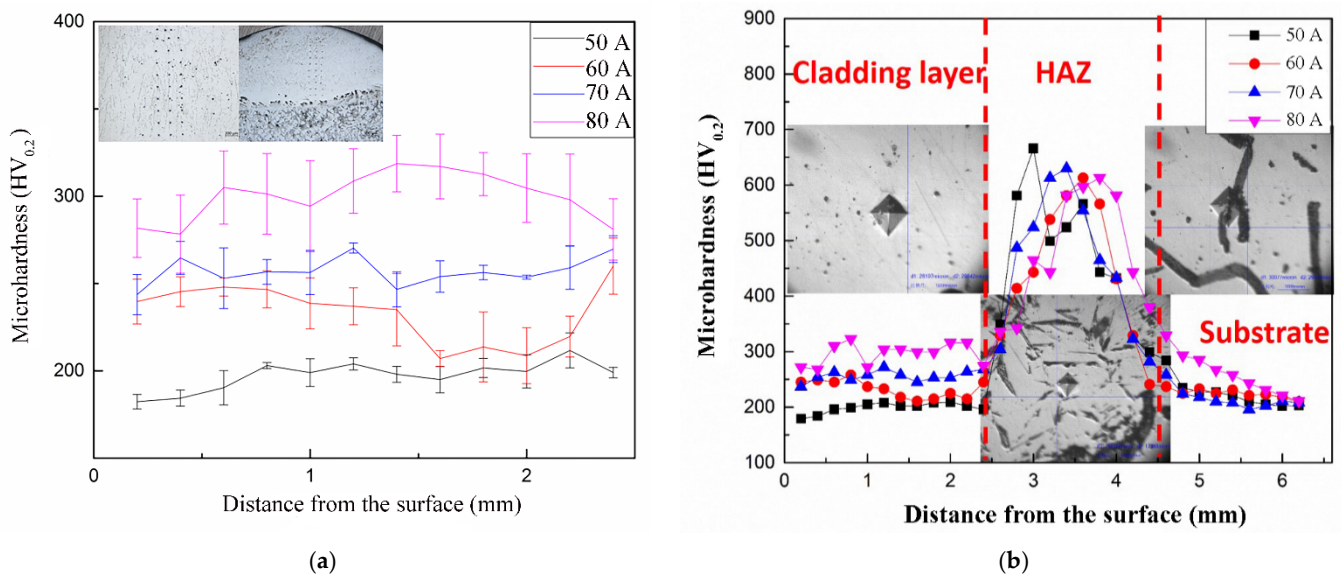


Figure 8. Microhardness of CoCrFeNiMn HEA coatings: (a) microhardness distribution along the top surface to the substrate across the cross-section of the HEA coatings, (b) microhardness distribution along the top surface to the substrate.

Table 6. Grain width of dendritic structure at different plasma currents.

Plasma Current/A	Dendritic Crystal Width/ μm
50 A	120 ± 42
60 A	43 ± 25
70 A	16 ± 4
80 A	6 ± 2

3.4. Electrochemical Corrosion

Figure 9 shows the polarization curves of CoCrFeNiMn HEA coatings prepared at different plasma currents in 3.5 wt.% NaCl solution. Table 7 shows the polarization curve fitting data for the tested samples according to the polarization curves in Figure 9 and the Tafel epitaxial tangent method for corrosion potential (E_{corr}), and corrosion current density (I_{corr}). According to the potential polarization curves, the self-corrosion potentials of the CoCrFeNiMn HEA coatings prepared at four different plasma currents were higher than that of the grey cast iron substrate. Therefore, the CoCrFeNiMn HEA coatings had better corrosion resistance than the grey cast iron and could effectively protect the grey cast iron from corrosion.

The CoCrFeNiMn HEA coating prepared at a plasma current of 60 A had the most positive corrosion potential, with E_{corr} of -0.253 VSCE and the lowest corrosion current density, with I_{corr} of 9.075×10^{-7} mA·mm⁻². With the increase of the plasma arc current, although the heating rate and the cooling rate increased simultaneously, the cooldown time was prolonged. During this period, the inter-dendritic structure grew. The inter-dendrite was enriched with Fe and Cr elements, and the dendrite was enriched with Co and Ni elements, which resulted in the differences of electrochemical properties between the grain and grain boundaries and furtherly formed the primary cell structure so that its corrosion resistance reduced gradually. Generally, the corrosion potential reflected the corrosion tendency of the material. The higher the corrosion potential, the higher the corrosion resistance. The lower the corrosion tendency, the lower the corrosion rate [34]. According to the experimental results, the CoCrFeNiMn HEA coating prepared at a plasma arc current of 60 A had the best corrosion resistance and the lowest corrosion rate.

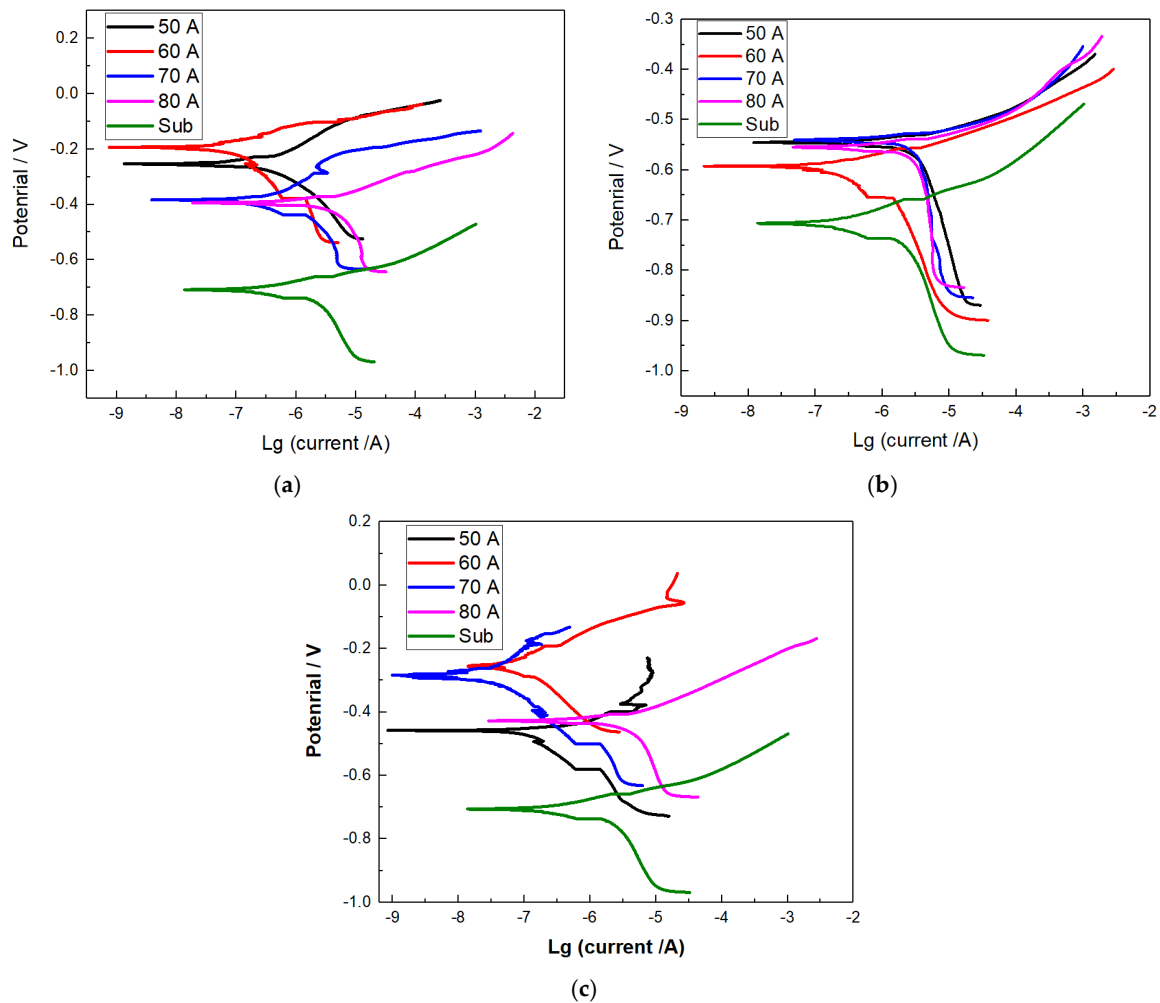


Figure 9. Polarization curves of substrate and HEA coatings in different zones: (a) bonding zone, (b) Heat affected zone and (c) coating zone.

Table 7. Self-corrosion potential and current density of the HEA coatings.

Zone	Plasma Current/A	50	60	70	80
Bonding Zone	E_{corr}/V	-0.25 ± 0.08	-0.294 ± 0.10	-0.387 ± 0.03	-0.391 ± 0.05
	$I_{\text{corr}}/\text{mA}\cdot\text{mm}^{-2}$	$1.085 \pm 0.3 \times 10^{-6}$	$5.37 \pm 0.7 \times 10^{-6}$	$3.596 \pm 0.6 \times 10^{-6}$	$1.36 \pm 0.08 \times 10^{-6}$
Heat Affected Zone	E_{corr}/V	-0.545 ± 0.04	-0.592 ± 0.12	-0.539 ± 0.07	0.0554 ± 0.007
	$I_{\text{corr}}/\text{mA}\cdot\text{mm}^{-2}$	$7.53 \pm 0.2 \times 10^{-7}$	$1.357 \pm 0.3 \times 10^{-6}$	$3.046 \pm 0.03 \times 10^{-6}$	$2.903 \pm 0.4 \times 10^{-6}$
Coating Zone	E_{corr}/V	-0.284 ± 0.01	-0.253 ± 0.05	-0.458 ± 0.009	-0.428 ± 0.08
	$I_{\text{corr}}/\text{mA}\cdot\text{mm}^{-2}$	$9.206 \pm 0.14 \times 10^{-7}$	$9.075 \pm 0.06 \times 10^{-7}$	$5.295 \pm 0.12 \times 10^{-6}$	$1.81 \pm 0.18 \times 10^{-6}$

Figure 10 shows the microstructure of the polished upper surface part in the CoCr-FeNiMn HEA coatings prepared at 50, 60, 70 and 80 A plasma arc currents subjected to potentiodynamic polarization corrosion tests. The HEA coatings with dendritic microstructures prepared at 70 and 80 A plasma arc currents experienced relatively severe corrosion in the electrochemical tests. The dendritic boundaries were deeply corroded. In contrast, HEA coatings without dendritic microstructures prepared at 50 A and 60 A plasma arc currents experienced relatively mild corrosion in the electrochemical tests. The complete solid solution had better corrosion resistance than the dendrites. The inter-dendritic microstructure was corroded and white materials precipitated between the dendrites, as shown by arrows in Figure 10c,d. The dendrites had better corrosion resistance than inter-dendrites. The corrosion-resistant elements migrated from inter-dendritic locations to the dendritic region

during the cladding processing. As shown in Figure 5, Cr element was enriched in the inter-dendrite zone and Ni, Co were enriched in the dendrites.

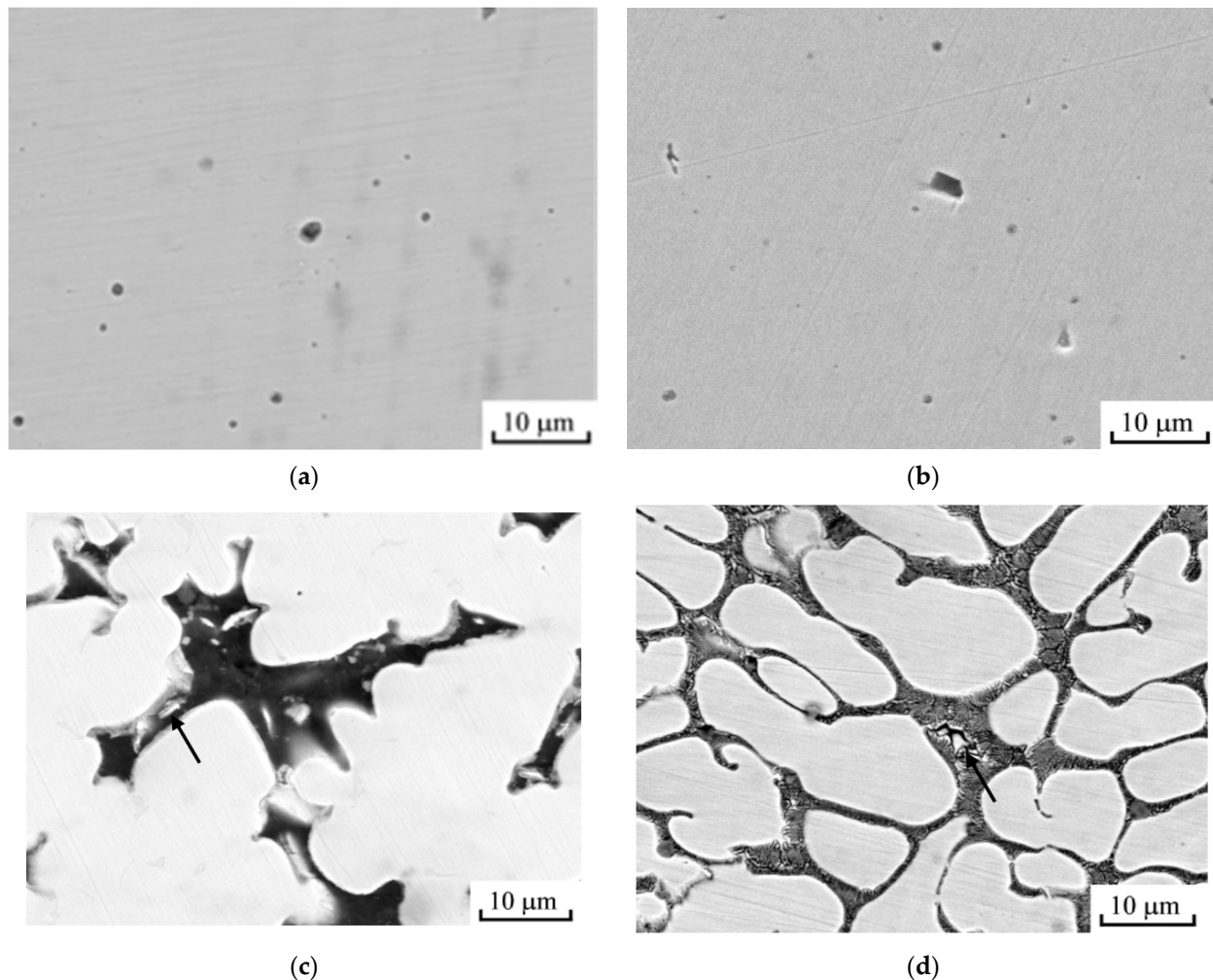


Figure 10. Microstructure of the polished upper surface part in the CoCrFeNiMn HEA coatings after corrosion test: (a) 50 A, (b) 60 A, (c) 70 A and (d) 80 A.

There were martensite (M), CoCrFeNiMn solid solution and ledeburite (L) in the bonding zone (BZ). The free corrosion potentials of the four bonding zones in the HEA coatings were all higher than the grey cast iron's, as seen in Figure 9a and Table 7. Especially, the free corrosion potential of the bonding zone (BZ) in the HEA coating prepared at 60 A plasma current was even higher than that of the HEA coatings, which might be attributed to the higher free corrosion potentials of martensite (M) and ledeburite (L) than CoCrFeNiMo solid solution [35,36].

The heat-affected zones (HAZ) in the four HEA coatings had comparable free corrosion potentials, which were higher than the grey cast iron's and lower than HEA coatings'. The heat affected zones (HAZ) experienced heat transfer to the inside of the grey cast iron at high temperature during the heating process by the plasma torch. There pearlite (P) was partially transformed into martensite (M), which improved the corrosion resistance significantly.

Therefore, by combining the corrosion potential (E_{corr}) and corrosion current density (I_{corr}) of the coating and bonded area, the CoCrFeNiMn HEA coating prepared at 60 A plasma current had the best corrosion resistance.

Figure 11 shows the schematic of the corrosion process of CoCrFeNiMn HEA coating in 3.5 wt.% NaCl solution. Cl⁻ had a strong adsorption ability on the alloy surface, which could accelerate the electrochemical reaction and corrosion rate. Therefore, when the

self-corrosion process started, the surface of the alloy did not have enough time to form an effective passivation film in a short time [37]. Cl⁻ rapidly penetrated the surface of the CoCrFeNiMn HEA coating and the alloy quickly reached the break-down potential, causing pitting corrosion. Moreover, solid solutions were not easier to be corroded by Cl⁻ as compared to the elemental substance. As seen in Figure 7, the CoCrFeNiMn HEA coatings had only a single FCC solid solution phase. Meanwhile, the contents of Co and Cr in the grain boundaries were higher than those in the grains as seen in Figures 5 and 6 and Table 4, which indicated that Co and Cr de-soluted from the single FCC solid solution partially along the grain boundaries. The precipitated elements might form intermetallic compounds or an amorphous phase. There were no obvious diffraction peaks broadening nor formation of intermetallic peaks, therefore, Co and Cr could be seen as a simple substance in the grain boundaries. As Cr had more negative electrical potential than Co, Cr was preferred to be corroded to form a passive film, which could inhibit the further corrosion. Therefore, the CoCrFeNiMn HEA coating prepared at a plasma arc current of 60 A had the best corrosion resistance and the lowest corrosion rate.

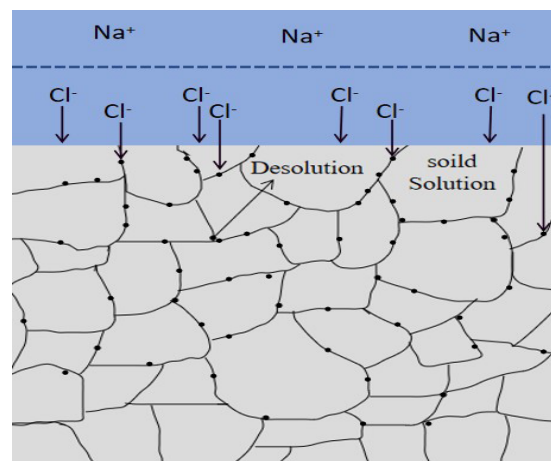


Figure 11. Schematic of the corrosion process of CoCrFeNiMn HEA coating in 3.5 wt.% NaCl solution.

Figure 12a shows the impedance spectra (Nyquist plot) of the coatings at different plasma arc currents. The fitted equivalent circuit was given out in Figure 12b. Table 8 shows the equivalent circuit parameters of CoCrFeNiMn HEA coatings. The impedances of the samples were fitted through ZView software[®]. Equation (2) reflected the fitted equivalent circuit relations.

$$Z(f) = R_s + \frac{R_1}{1 + j2\pi f R_1 C_1} + \frac{R_t}{R_t Q (j2\pi f)^\alpha + 1} + \frac{R_2}{1 + j2\pi f R_2 C_2} \quad (2)$$

where, R_1 and R_2 were corrosion product resistance; R_s was the solution resistance in the electrochemical reaction system; R_t was the substrate interface charge transfer resistance in 3.5 wt.% NaCl solution; C_1 and C_2 denoted the sample interface capacitance; Q was the physical quantity used to describe the deviation of the parameters of capacitance C , whose scale was $\Omega^{-1} \cdot \text{cm}^{-2} \cdot \text{s}^{-n}$ or $\text{S} \cdot \text{cm}^{-2} \cdot \text{s}^{-n}$; j was the imaginary unit $\sqrt{-1}$; f was the frequency (Hz, s^{-1}) and α had the meaning that in the Cole-Cole diagram ($\epsilon'' - \epsilon'$ diagram), $\frac{\pi}{2}\alpha$ was the angle between the intercept point at the real axis and the center of the circle and the real axis at high frequencies.

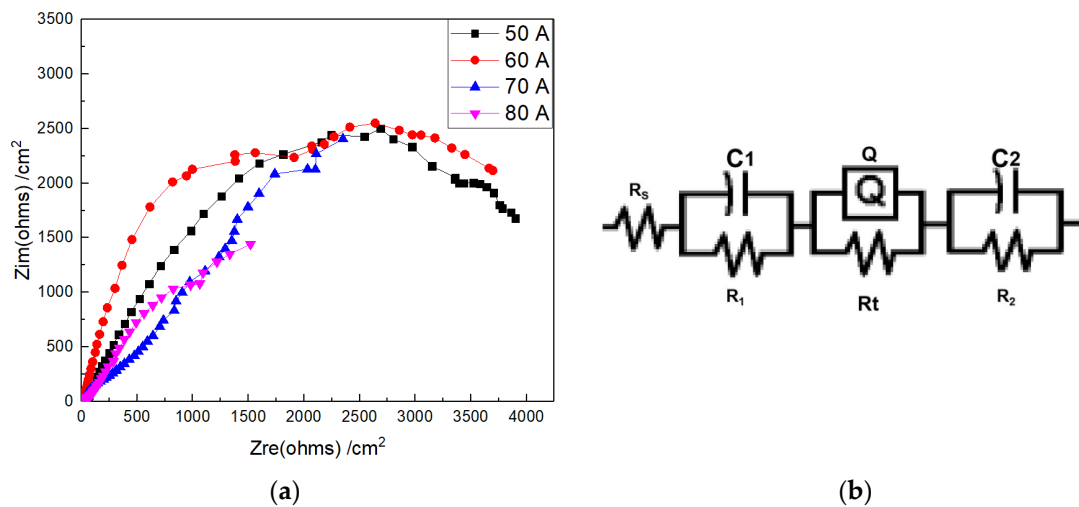


Figure 12. Electrochemical impedance spectroscopy in the middle of the CoCrFeNiMn HEA coatings (a), and the equivalent fitting circuit (b).

Table 8. Equivalent circuit parameters of the CoCrFeNiMn HEA coatings.

Coatings Deposition Plasma Arc Current/A	R_s/Ω	C_1/C	R_1/Ω	Q/C	n	R_t/Ω	C_2/C	R_2/Ω
50	18.86 ± 1.2	$1.142 \pm 0.5 \times 10^{-3}$	541.1 ± 5.2	$2.253 \pm 0.12 \times 10^{-4}$	0.6824 ± 0.13	5073 ± 25	$7.745 \pm 0.21 \times 10^{-4}$	16.48 ± 2.21
60	14.79 ± 0.8	$5.006 \pm 0.3 \times 10^{-4}$	153.7 ± 8.2	$5.235 \pm 0.22 \times 10^{-4}$	0.5998 ± 0.08	9711 ± 46	$4.04 \pm 0.11 \times 10^{-4}$	200.8 ± 13.2
70	15.35 ± 1.0	$2.599 \pm 0.8 \times 10^{-5}$	7.126 ± 1.0	$1.629 \pm 0.08 \times 10^{-4}$	0.685 ± 0.21	6043 ± 16	$6.471 \pm 0.12 \times 10^{-5}$	63.48 ± 1.36
80	14.20 ± 1.3	$2.334 \pm 1.0 \times 10^{-5}$	13.03 ± 0.6	$1.631 \pm 0.26 \times 10^{-4}$	0.7025 ± 0.14	5672 ± 25	$2.418 \pm 0.176 \times 10^{-4}$	670.2 ± 9.86

According to the EIS results, an electrical equivalent circuit (EC) could be fitted to simulate the electrolyte/sample interface. As shown in Figure 12b, the EC could be used to trace the corrosion of the metal coated surface. The CoCrFeNiMn HEA surface was divided into three distinguishable parts. The first part of the surface was covered with a protective passive layer, the second part was the area of the surface without passivation film and the third part was the vulnerable area where pits tended to form due to Cr depletion and/or surface defects [38]. On the passive surface, the equivalent circuit consisted of the solution resistance (R_s), the charge transfer resistance (R_t) and the capacitance of the passivation film protective layer (C_1). R_s was the solution resistance between the electrode in the pitting state and the reference electrode. R_1 and C_1 were the polarization resistance and capacitance of the passivation surface, respectively. Meanwhile, their parallel connection could be used to describe the charge transfer process in the passive layer on the coating surface. R_t was the charge transfer resistance at the substrate interface in a 3.5 wt.% NaCl solution and could be used in parallel with Q to describe the charge transfer process in the unpassivated area of the coating. R_2 and C_2 were the resistance and capacitance of the vulnerable area, where Cr depleted and/or surface defects and pits tended to form, respectively. R_2 showed the charge transfer on the crater wall and C_2 explained the “porosity” caused by the crater [39].

In the CoCrFeNiMn system, the standard electrode potentials of Co, Cr, Fe, Ni and Mn were -0.277 V, -0.74 V, -0.44 V, -0.25 V and -1.179 V, respectively. Co and Ni had higher electrical potential than Fe, Cr and Mn. Fe, Cr, Mn have three lower electrical potential elements could easily form a primary cell.

The coatings at different plasma arc currents exhibited different diameters of capacitive arcs, which indicated that the four groups of coated specimens had the same corrosion mechanism but different corrosion rates. In general, the diameter of the capacitive arc reflected the magnitude of the charge transfer resistance (R_t), which indicated the corrosion resistance of the material. With the increase of the diameter of the capacitive arc, the charge transfer difficulty increased and the corrosion rate decreased [40]. As seen in Figure 12

and Table 8, the charge transfer resistances (R_t) of the CoCrFeNiMn HEA coatings were sorted from high to low in the following order: coatings prepared at 60, 70, 50 and 80 A. Therefore, the HEA coating prepared at 60 A plasma current had the highest charge transfer resistances for a single FCC solid solution phase and the relative higher concentration of Cr in the grain boundaries than in the grains. Combined with the polarization curve results, the HEA coating prepared at 60 A plasma current had the best corrosion resistance and could afford the best protection for the grey cast iron substrate.

4. Conclusions

CoCrFeNiMn high-entropy alloy coatings were deposited on grey cast iron through plasma transfer arc cladding. There were fine acicular martensite and ledeburite in the bonding zone, columnar grains perpendicular to the interface between grey cast iron substrate and cladding, as well as dendrite in the middle part of the coatings. Simple FCC solid solutions existed in the coatings, which were similar to the powder's structure. The coating had the highest microhardness of $300 \pm 21.5 \text{ HV}_{0.2}$ when the plasma current was 80 A for the solid solution strengthening, while, the HEA coating had the highest corrosion potential of -0.253 V when the plasma current was 60 A, which was much higher than the grey cast iron's corrosion potential of -0.708 V . Meanwhile, the coating had a much lower corrosion current density of $9.075 \times 10^{-7} \text{ mA/cm}^2$ than the grey cast iron's $2.4825 \times 10^{-6} \text{ mA/cm}^2$. The CoCrFeNiMn HEA coating had much better corrosion resistance and lower corrosion rate than the grey cast iron for single FCC solid solution phase and the relative higher concentration of Cr in the grain boundaries than in the grains and could display good corrosion protecting effects.

Author Contributions: Conceptualization, P.-H.G., R.-T.F., S.-C.Z. and M.-X.L.; methodology, P.-H.G., R.-T.F., S.-C.Z., B.-Y.C., M.-X.L., L.J. and D.Z.; software, P.-H.G., R.-T.F., S.-C.Z. and Y.-C.G.; validation, P.-H.G. and S.-C.Z.; formal analysis, P.-H.G., R.-T.F. and S.-C.Z.; investigation, P.-H.G., R.-T.F., S.-C.Z., B.Z., B.-Y.C., Y.-Q.L., L.J. and D.Z.; data curation, Z.Y.; writing—original draft preparation, R.-T.F.; writing—review and editing, P.-H.G.; simulation, R.-T.F. and Y.-C.G.; experiment, R.-T.F. and B.Z.; project administration, J.-P.L.; funding acquisition, P.-H.G. and J.-P.L. All authors have read and agreed to the published version of the manuscript.

Funding: This work was funded by the National Natural Science Foundation of China (51771140), China Scholarship Council (201908610115), Shaanxi Key Science and Technology Innovation Team (2017KCT-05), The Youth Innovation Team of Shaanxi Universities: Metal Corrosion Protection and Surface Engineering Technology, Shaanxi Provincial Key Research and Development Project (2019ZDLGY05-09), Local Serving Special Scientific Research Projects of Shaanxi Provincial Department of Education (19JC022), Project of Yulin Science and Technology Bureau (2019-121).

Institutional Review Board Statement: Not applicable.

Informed Consent Statement: Not applicable.

Data Availability Statement: Not applicable.

Conflicts of Interest: The authors declare no conflict of interest.

References

1. Yeh, J.W.; Chen, S.K.; Lin, S.J.; Gan, J.Y.; Chin, T.S.; Shun, T.T.; Tsau, C.H.; Chang, S.Y. Nanostructured high-entropy alloys with multiple principal elements: Novel alloy design concepts and outcomes. *Adv. Eng. Mater.* **2004**, *6*, 299–303. [[CrossRef](#)]
2. Feng, X.R.; Cui, X.F.; Jin, G.; Zheng, W.; Cai, Z.B.; Wen, X.; Lu, B.W.; Li, J.M. Underwater laser cladding in full wet surroundings for fabrication of nickel aluminum bronze coatings. *Surf. Coat. Technol.* **2018**, *333*, 104–114. [[CrossRef](#)]
3. Yang, T.; Zhao, Y.; Tong, Y.; Jiao, Z.; Wei, J.; Cai, J.; Han, X.; Chen, D.; Hu, A.; Kai, J.; et al. Multicomponent intermetallic nanoparticles and superb mechanical behaviors of complex alloys. *Science* **2018**, *362*, 933–937. [[CrossRef](#)] [[PubMed](#)]
4. Fu, Z.; Jiang, L.; Wardini, J.L.; MacDonald, B.E.; Wen, H.; Xiong, W.; Zhang, D.; Zhou, Y.; Rupert, T.J.; Chen, W.; et al. A high-entropy alloy with hierarchical nanoprecipitates and ultrahigh strength. *Sci. Adv.* **2018**, *4*, 8712. [[CrossRef](#)] [[PubMed](#)]
5. Zou, Y.; Ma, H.; Spolenak, R. Ultrastrong ductile and stable high-entropy alloys at small scales. *Nat. Commun.* **2015**, *6*, 7748. [[CrossRef](#)] [[PubMed](#)]

6. Yao, Y.; Huang, Z.; Xie, P.; Lacey, S.D.; Jacob, R.J.; Xie, H.; Chen, F.; Nie, A.; Pu, T.; Rehwoldt, M.; et al. Carbothermal shock synthesis of high-entropy-alloy nanoparticles. *Science* **2018**, *359*, 1489–1494. [[CrossRef](#)]
7. El-Atwani, O.; Li, N.; Li, M.; Devaraj, A.; Baldwin, J.K.S.; Schneider, M.M.; Sobieraj, D.; Wróbel, J.S.; Nguyen-Manh, D.; Maloy, S.A.; et al. Outstanding radiation resistance of tungsten-based high-entropy alloys. *Sci. Adv.* **2019**, *5*, 2002. [[CrossRef](#)]
8. Qiu, Y.; Thomas, S.; Gibson, M.A.; Fraser, H.L.; Birbilis, N. Corrosion of high entropy alloys. *NPJ Mater. Degrad.* **2017**, *1*, 15. [[CrossRef](#)]
9. Chuang, M.; Tsai, M.; Wang, W.; Lin, S.; Yeh, J. Microstructure and wear behavior of Al_xCo_{1.5}CrFeNi_{1.5}Ti_y high-entropy alloys. *Acta Mater.* **2011**, *59*, 6308–6317. [[CrossRef](#)]
10. Piglione, A.; Dovggy, B.; Liu, C.; Gourlay, C.M.; Hooper, P.A.; Pham, M.S. Printability and microstructure of the CoCrFeMnNi high-entropy alloy fabricated by laser powder bed fusion. *Mater. Lett.* **2018**, *224*, 22–25. [[CrossRef](#)]
11. Yim, D.; Sathiyamoorthi, P.; Hong, S.J.; Kim, H.S. Fabrication and mechanical properties of TiC reinforced CoCrFeMnNi high-entropy alloy composite by water atomization and spark plasma sintering. *J. Alloys Compd.* **2019**, *781*, 389–396. [[CrossRef](#)]
12. Lai, C.H.; Lin, S.J.; Yeh, J.W.; Chang, S.Y. Preparation and Characterization of AlCrTaTiZr Multi-Element Nitride Coatings. *Surf. Coat. Technol.* **2006**, *20*, 3275. [[CrossRef](#)]
13. Chen, T.K.; Shun, T.T.; Yeh, J.W.; Wong, M.S. Nanostructured Nitride Films of Multi-Element High-Entropy Alloys by Reactive DC Sputtering. *Surf. Coat. Technol.* **2004**, *188*, 189–193. [[CrossRef](#)]
14. Meghwal, A.; Anupam, A.; Murty, B.S.; Berndt, C.C.; Ang, A. Thermal Spray High-Entropy Alloy Coatings: A Review. *J. Therm. Spray. Technol.* **2020**, *29*, 857–893. [[CrossRef](#)]
15. Shu, F.; Wang, B.; Zhao, H.; Zhang, J. Effects of Line Energy on Microstructure and Mechanical Properties of CoCrFeNiBSi High-Entropy Alloy Laser Cladding Coatings. *J. Therm. Spray. Technol.* **2020**, *29*, 789–797. [[CrossRef](#)]
16. Ye, X.H.; Ma, M.X.; Cao, Y.X.; Liu, W.J.; Ye, X.H.; Gu, Y. The Property Research on High-entropy Alloy Al_xFeCoNiCuCr Coating by Laser Cladding. *Phys. Procedia.* **2011**, *12*, 303–312. [[CrossRef](#)]
17. Lehtonen, J.; Koivuluoto, H.; Ge, Y.; Juselius, A.; Hannula, S.P. Cold Gas Spraying of a High-Entropy CrFeNiMn Equiatomic. *Alloy. Coat.* **2020**, *10*, 53. [[CrossRef](#)]
18. Chen, L.J.; Bobzin, K.; Zhou, Z.; Zhao, L.D.; Mehmet, Ö.; Tim, K.; Tan, Z.; He, D.Y. Wear behavior of HVOF-sprayed Al_{0.6}TiCrFeCoNi high entropy alloy coatings at different temperatures. *Surf. Coat. Technol.* **2019**, *358*, 215–222. [[CrossRef](#)]
19. Zhang, J.; Liu, M.; Song, J.; Deng, C.; Deng, C. Microstructure and corrosion behavior of Fe-based amorphous coating prepared by HVOF. *J. Alloys Compd.* **2017**, *721*, 506–511. [[CrossRef](#)]
20. Zhang, B.S.; Cheng, J.B.; Xu, B.S. (CuCoCrFeNi)₉₅B₅ hightentropy alloy coatings prepared by plasma transferred arc cladding process. *Rare Metal Mater. Eng.* **2014**, *43*, 1128–1132.
21. Kim, Y.S.; Park, H.J.; Mun, S.C.; Jumaev, E.; Hong, S.H.; Song, G.; Kim, J.T.; Park, Y.K.; Kim, K.S.; Jeong, S.I.; et al. Investigation of structure and mechanical properties of TiZrHfNiCuCo high entropy alloy thin films synthesized by magnetron sputtering. *J. Alloys Compd.* **2019**, *797*, 834–841. [[CrossRef](#)]
22. Lin, T.S.; He, P.; Wang, X.R.; Wang, Z.Q.; Shi, Y. Microstructure and wear properties of CuNiSiTiZr high-entropy alloy coatings on TC11 titanium alloy produced by eletrospark-computer numerical control deposited process. *Surf. Coat. Technol.* **2015**, *283*, 156–161.
23. Cheng, J.B.; Liu, D.; Liang, X.B.; Chen, Y.X. Evolution of microstructure and mechanical properties of in situ synthesized TiC-TiB₂/CoCrCuFeNi high entropy alloy coatings. *Surf. Coat. Technol.* **2015**, *281*, 109–116. [[CrossRef](#)]
24. Sudha, C.; Shankar, P.; Rao, R.V.S.; Thirumurugesan, R.; Vijayalakshmi, M.; Raj, B. Microchemical and microstructural studies in a PTA weld overlay of Ni–Cr–Si–B alloy on AISI 304L stainless steel. *Surf. Coat. Technol.* **2008**, *202*, 2103–2112. [[CrossRef](#)]
25. Stern, M.; Geary, A.L. Electrochemical polarization I. A theoretical analysis of the shape of polarization curves. *J. Electrochem. Soc.* **1957**, *104*, 56. [[CrossRef](#)]
26. Liu, M.J.; Zhang, G.; Lu, Y.H.; Han, J.Q.; Li, G.R.; Li, C.J.; Yang, G.J. Plasma spray-physical vapor deposition toward advanced thermal barrier coatings: A review. *Rare Metals* **2020**, *39*, 479–497. [[CrossRef](#)]
27. Lin, D.Y.; Zhang, N.N.; He, B.; Gong, X.; Gong, X.; Zhang, Y.; Li, D.Y.; Dong, F.Y. Structural Evolution and Performance Changes in FeCoCrNiAlNb_x High-Entropy Alloy Coatings Cladded by Laser. *J. Therm. Spray. Technol.* **2017**, *26*, 2005–2012. [[CrossRef](#)]
28. Zhang, W.R.; Peter, K.L.; Zang, Y. Science and technology in high-entropy alloys. *Sci. China Mater.* **2018**, *1*, 1–21. [[CrossRef](#)]
29. Wang, C.L.; Gao, Y.; Wang, R.; Wei, D.Q.; Cai, M.; Fu, Y.K. Microstructure of laser-clad Ni60 cladding layers added with different amounts of rare-earth oxides on 6063 Al alloys. *J. Alloys Compd.* **2018**, *740*, 1099–1107. [[CrossRef](#)]
30. Kiviy, B.M.; Zaeem, A. Generalized stacking fault energies, ductilities, and twinnabilities of CoCrFeNi-based face-centered cubic high entropy alloys. *Scr. Mater.* **2017**, *139*, 83–86. [[CrossRef](#)]
31. Wu, W.; Jiang, L.; Jiang, H.; Pan, X.M.; Cao, Z.Q.; Deng, D.W.; Wang, T.M.; Li, T.J. Phase Evolution and Properties of Al₂CrFeNiMo_x High-Entropy Alloys Coatings by Laser Cladding. *J. Therm. Spray. Technol.* **2015**, *24*, 1333–1340. [[CrossRef](#)]
32. Gao, P.H.; Chen, B.Y.; Zhang, B.; Yang, Z.; Guo, Y.C.; Li, J.P.; Liang, M.X.; Li, Q.P. Preparations of iron-based alloy coatings on grey cast iron through plasma transfer arc welding. *J. Adhes. Sci. Technol.* **2021**. [[CrossRef](#)]
33. Gao, P.H.; Chen, B.Y.; Zeng, S.C.; Yang, Z.; Guo, Y.C.; Liang, M.X.; Xu, T.; Li, J.P. Effect of Vacuum Annealing on the Nickel-Based Coatings Deposited on a CGI Cast Iron through Atmospheric Plasma Spraying. *Metals* **2020**, *10*, 963. [[CrossRef](#)]
34. Kaseem, M.; Ko, Y.G. Formation of flower-like structures for optimizing the corrosion resistance of Mg alloy. *Mater. Lett.* **2018**, *221*, 196–200. [[CrossRef](#)]

35. Shi, Y.Z.; Yang, B.; Liaw, P.K. Corrosion resistant high entropy alloys: A review. *Metals* **2013**, *7*, 43. [[CrossRef](#)]
36. Liu, J.; LI, J.; Cheng, X.; Wang, H. Effect of dilution and macro-segregation on corrosion resistance of laser clad AerMet100 steel coating on 300M steel substrate. *Surf. Coat. Technol.* **2017**, *325*, 352–359. [[CrossRef](#)]
37. Song, C.H.; Gan, Z.H.; Lu, Z.H.; Chen, H.J.; Huang, F. Preparation and electrochemical properties of AlMgZnSnPbCuMnNi high entropy alloys with low free corrosion potentials. *J. Mater. Sci. Eng.* **2011**, *29*, 747–752.
38. Gao, J.; Jiang, Y.; Deng, B.; Zhang, W.; Zhong, C.; Li, J. Investigation of selective corrosion resistance of aged lean duplex stainless steel 2101 by non-destructive electrochemical techniques. *Electrochim. Acta* **2009**, *54*, 5830–5835. [[CrossRef](#)]
39. Hitz, C.; Lasia, A. Experimental study and modeling of impedance of the her on porous Ni electrodes. *J. Electroanal. Chem.* **2001**, *500*, 213–222. [[CrossRef](#)]
40. Niu, B.; Shi, P.; E, S.S.; Wei, D.H.; Li, Q.; Chen, Y. Preparation and characterization of HA sol–gel coating on MAO coated AZ31 alloy. *Surf. Coat. Technol.* **2016**, *286*, 42–48. [[CrossRef](#)]